ACS Photonics

Open Access

This article is licensed under CC-BY-NC-ND 4.0

pubs.acs.org/journal/apchd5

Article

Multiscale Chirality in Moiré Metasurfaces Revealed by Terahertz Circular Dichroism Spectroscopic Imaging

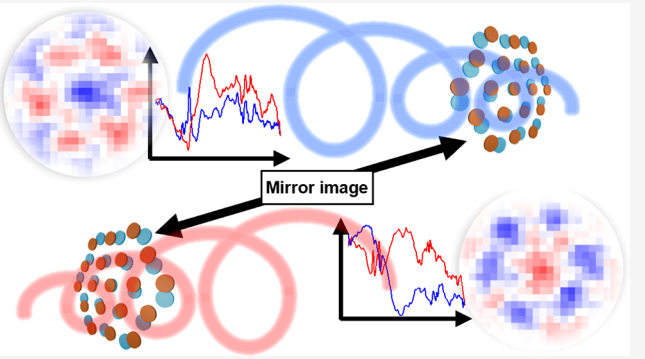
Uina Chiba, Shota Tsuji, Gaku Oritani, Takumi Yoichi, Rinpei Sasaki, Takeo Minari, Seigo Ohno, and Katsuhiko Miyamoto*

Cite This: *ACS Photonics* 2026, 13, 3357−3368

Read Online

ACCESS | Metrics & More | Article Recommendations

ABSTRACT: Terahertz circular dichroism (THz-CD) spectroscopy provides unique access to low-energy chiral interactions between circularly polarized THz light and multiscale chirality in materials. Yet it has remained unclear whether the THz band can function as a practical, high-fidelity probe that produces visualization of spatial distribution of such interactions. Here, we establish that it can by introducing a frequency-tunable THz-CD spectroscopic imaging platform operating across 3−6 THz with narrow spectral bandwidth, circularly polarized excitation, and two-dimensional readout. Using twisted-layer moiré metasurfaces (TMMSs) as a top-down, reconfigurable model system that allows deterministic design and control of chirality—in contrast to bottom-up chiral media such as biomolecules, whose handedness is constrained by biochemical stability—we spatially resolve chiral responses that elude spatially averaged spectra: the dissymmetry (*g*-factor) inverts sign between topological singularities within a single planar architecture and reverses with the twist handedness, whereas scale moiré counterparts remain achiral. We formulate complementary indicators for local displacement asymmetry and macroscopic rotational geometry and show that only their combined action reproduces the measured 2D images, thereby providing experimental validation of a multiscale description in the THz regime. Beyond this platform, our results position spatial THz-CD imaging (3−6 THz) as a practical tool for site-specific chiral metrology in metasurfaces, soft-phonon materials, and biomolecular assemblies.



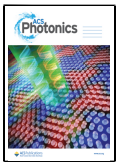
KEYWORDS: *terahertz frequency, circular dichroism, spectroscopy, imaging, multiscale chirality, metasurface*

1. INTRODUCTION

Circular dichroism (CD) probes[1,2] spin-selective light−matter interactions using left- and right-handed circularly polarized (LCP and RCP) light and has illuminated chirality across chemistry, materials, and biophotonics.[3−8] In addition to spin-selective absorption, chiral materials can profoundly modulate electromagnetic responses and enable unconventional control over light−matter interactions, as demonstrated in diverse chiral systems.[9] The terahertz (THz) band (0.1−10 THz; 0.4−40 meV) hosts low-energy collective motions[10−12]—intermolecular vibrations, phonons, and large-amplitude torsions—that are exquisitely sensitive to molecular and mesoscale structure. Consequently, THz frequencies are increasingly recognized as a critical window for accessing three-dimensional (3D) structural chirality and anisotropy that remain elusive to conventional optical probes. Yet a practical, spatially resolved chiroptical probe in the THz band has been missing: most THz-CD implementations have been spectral/point measurements with limited tunability and are effectively restricted to spatially uniform samples, typically operating below ∼3 THz.[1,10,13−15] Here we close this gap by developing a frequency-tunable THz-CD spectroscopic imaging platform that operates across 3−6 THz with narrowband, polarization-pure excitation and 2D readout. Restricting ourselves to circularly polarized THz light (spin angular momentum) isolates the spin degree of freedom, while raster scanning yields spatial maps of the CD dissymmetry (*g*-factor) over millimeter-scale areas with ∼100 μm sampling. This establishes the THz band as a practical, high-fidelity probe capable of producing 2D chiroptical images rather than spatially averaged spectra.

A second obstacle has been model availability. Chirality exhibits multiscale behavior across different molecular structural scales, a phenomenon well-known in biomaterials

Received: February 12, 2026
Revised: May 6, 2026
Accepted: May 7, 2026
Published: June 2, 2026



© 2026 The Authors. Published by American Chemical Society

Downloaded from pubs.acs.org/apchd5/article-pdf/13/12/3357/6626029/acsphotonics.6c00372.pdf by NATL INST FOR MATLS SCIENCE (NIMS) user on 12 November 2026

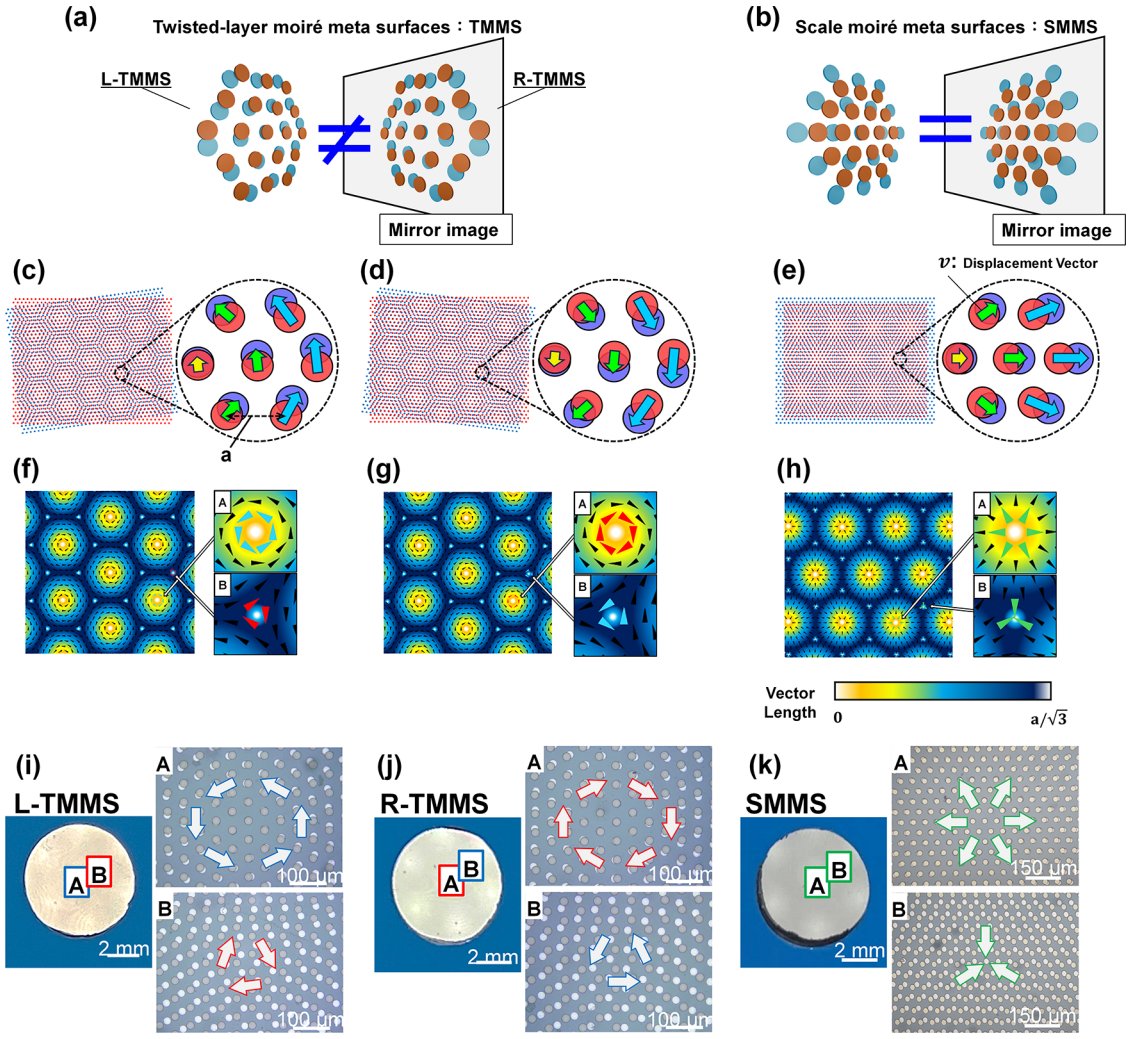


Figure 1. Schematic diagrams of (a) TMMS and (b) SMMS configurations. (c–e) Definition and spatial mapping of in-plane displacement vector $\boldsymbol{v}$ for (c) L-TMMS, (d) R-TMMS, and (e) SMMS. (f–h) Corresponding displacement vector fields for (c–e), with color and arrows indicating magnitude and direction, respectively. Topological singularities A and B, where $\boldsymbol{v}$ is undefined, are observed in the L-TMMS, R-TMMS, and SMMS. (i–k) Optical and microscopic images of the fabricated (i) L-TMMS, (j) R-TMMS, and (k) SMMS. The arrows indicate the orientation of the displacement vector around singularities A and B: clockwise and anticlockwise rotations in the TMMS are shown in red and blue, respectively, while the SMMS exhibits radial patterns indicated in green.

as seen in optically active molecules and protein helix structures. However, the mechanism governing the interaction between light and material chirality remains unclear. One reason for this is that in biological systems, molecular chirality is selected for biochemical stability, precluding free design and systematic study. Recent progress in chiral metasurfaces has demonstrated that structured optical fields can be engineered through nanoscale and mesoscale geometric design. While many of these advances have been achieved in the visible–infrared regimes, related developments in the THz domain have also begun to emerge.[16−18] However, two-dimensional, spatially resolved chiroptical imaging remains rare across all frequency ranges, not only in THz but also in optical and infrared bands, where most studies rely on spatially averaged CD spectra. Extending chiral-metasurface concepts into the THz band therefore requires an approach capable of resolving spatial chirality, rather than depending solely on point-based CD measurements. To address these limitations, we employ twisted-layer moiré metasurfaces (TMMSs) as a reconfigurable, top-down platform that encodes local displacement asymmetry and macroscopic rotational geometry in a single planar architecture and contains topological singularities where optical anisotropy becomes undefined. As an achiral control, scale moiré metasurfaces (SMMSs) preserve mirror symmetry around the singularities. This model pair enables site-specific interrogation of chiral responses that are otherwise hidden in averaged spectra. Since exact periodic boundary conditions—which can simplify theoretical frameworks and significantly reduce computational resources—cannot generally be applied to two-dimensional moiré patterns, particularly when multiple local configurations are involved, experimental approaches serve as an effective means for systematically investigating diverse chiral patterns.

With these tools and models in hand, we establish three findings that frame the remainder of the work. First, 2D THz-CD maps directly reveal site-specific handedness inversion between singularities within a single TMMS, and the entire contrast reverses with the global twist handedness, whereas SMMS counterparts remain near-zero in g-factor—demonstrating the sensitivity and selectivity of spin-based THz

https://doi.org/10.1021/acsphotonics.6c00372
ACS Photonics 2026, 13, 3357−3368

Downloaded from pubs.acs.org/apchd5/article-pdf/13/12/3357/6260299/acsphotonics.6c00372.pdf by NATL INST FOR MATLS SCIENCE (NIMS) user on 12 November 2026

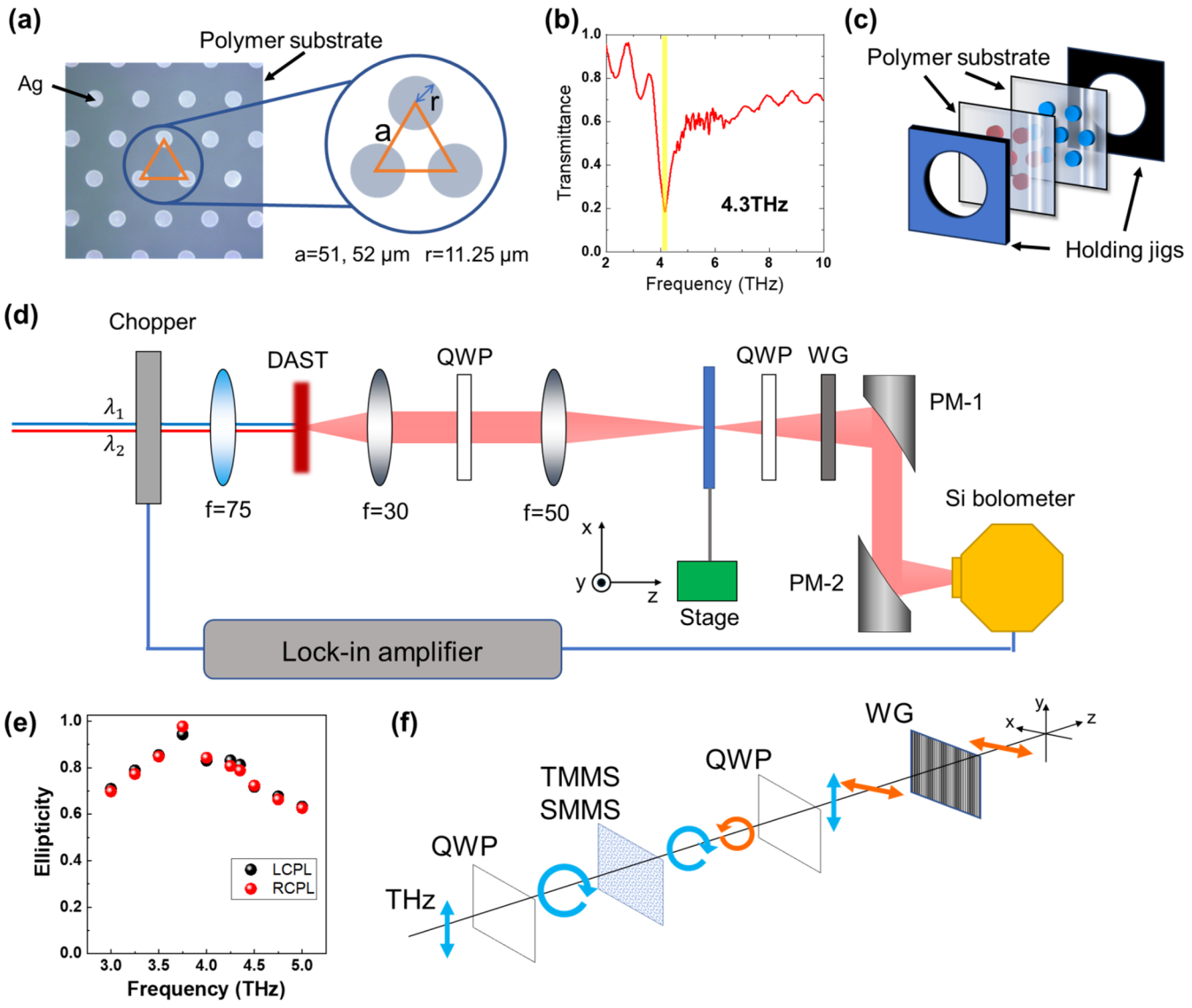


Figure 2. (a) Optical micrograph and schematic diagram of film-1, comprising a triangular lattice of silver disks fabricated on a 50 μm-thick Zeonor film via printed electronics. (b) THz-FTIR transmission spectrum of film-1, showing a dip near 4.3 THz corresponding to the lattice resonance of the metallic triangular lattice. (c) Sample configurations prepared by sandwiching films between holding jigs. (d) Experimental setup of THz-CD spectroscopic imaging system using DAST-DFG frequency-tunable THz source. (e) Measured circular polarization ellipticity as a function of THz frequency. (f) Circularly polarized crossed-Nicol detection scheme employing quarter-wave plate (QWP) and wire-grid (WG) analyzer.

imaging. Second, we construct complementary indicators that quantify local (unit-cell-level displacement asymmetry) and macroscopic (beam-integrated rotational field) chirality and show that only their combined action reproduces the measured images—thereby providing an experimental validation of a multiscale description in this frequency range. Third, by using a deterministic, top-down, reconfigurable platform rather than relying on bottom-up self-assembly, we supply a route to design, control, and benchmark multiscale chirality under spin-selective THz excitation. Together, these elements position spatial THz-CD imaging (3–6 THz) as a practical metrology for chiral photonics[19−22] and materials characterization.[23−25]

2. MOIRÉ-TYPE METASURFACES

TMMSs and SMMSs, which feature two-dimensionally distributed structures suitable for the spatial modulation of light, were employed as samples for THz-CD spectroscopic imaging. Metasurfaces, composed of subwavelength artificial structures, are widely used to manipulate electromagnetic waves.[26] Their compact nature enables control over various optical properties, including amplitude, phase, polarization, and frequency.[27,28] When two periodic structures are superimposed with a slight twist or displacement, a moiré superlattice emerges, producing a varying interference pattern. MMSs exploit this principle to couple moiré-induced anisotropy with electromagnetic waves. In our implementation, the MMS consists of metallic disk arrays arranged on a triangular lattice. A moiré pattern emerges when two such layers are superimposed with a slight relative displacement, resulting in structural chirality. We previously demonstrated[28] phase controllability in MMSs arising from localized and two-dimensional anisotropy. However, the structural chirality inherent to these configurations has remained largely unexplored. While earlier studies primarily addressed geometric phase effects, the present work focuses on the emergence of 3D chirality induced by stacked-layer arrangements.

https://doi.org/10.1021/acsphotonics.6c00372
ACS Photonics 2026, 13, 3357−3368

Downloaded from pubs.acs.org/apchd5/article-pdf/13/12/3357/6260299/acsphotonics.6c00372.pdf by NATL INST FOR MATLS SCIENCE (NIMS) user on 12 November 2026

Figure 1(a,b) schematically illustrate a TMMS and an SMMS, respectively. A TMMS is formed by rotating two metallic periodic structures with identical lattice constant a, allowing the definition of right- and left-handed configurations. In contrast, an SMMS comprises two periodic structures with different lattice constants, producing a scale moiré pattern. To visualize local anisotropy within the moiré pattern, we define an in-plane displacement vector $\boldsymbol{v}$ for each unit cell.[28] This vector extends from the center of a disk in the first layer to the nearest disk in the second layer. Figures 1 (c–e) depict the displacement vectors for a left-handed TMMS (L-TMMS), a right-handed TMMS (R-TMMS), and an SMMS, respectively, with vector length and direction indicated by color and arrows, respectively. The TMMSs and the SMMS exhibit topological singularities where the displacement vector is undefined, indicated as singularities A and B in Figure 1(f–h). Around these singularities, the phase changes by 4π and -2π, respectively. Such MMSs have been proposed for generating optical vortex arrays via geometric phase modulation.[29]

For a TMMS, stacking two achiral structures with a rotational operation breaks the global mirror symmetry of the system; this symmetry breaking also manifests locally. Singularities A and B act as centers of structural chirality. At singularity A of the L-TMMS (Figure 1(f)), the displacement vector $\boldsymbol{v}$ exhibits a 3D anticlockwise rotation from the first-layer disk toward the second-layer disk, whereas singularity B rotates clockwise. In the figure, left- and right-handed rotation is indicated by blue and red arrows, respectively. For the R-TMMS, the rotation directions are reversed: singularities A and B rotate clockwise and anticlockwise, respectively (Figure 1(g)).

In contrast, an SMMS involves a scaling operation that preserves global mirror symmetry; however, local mirror symmetry breaking still exists. The SMMS also contains singularities A and B where $\boldsymbol{v}$ is undefined; however, the surrounding regions lack any 3D chirality. As shown in Figure 1(h), the displacement vectors exhibit no rotational behavior but instead form a radial pattern, either diverging from singularity A or converging toward singularity B, resulting in mirror symmetry. This radial configuration underscores the fundamental difference between SMMSs and TMMSs: unlike TMMSs, SMMSs do not exhibit twist-induced chirality at singularities.

To complement the schematic displacement-vector fields in Figure 1(f–h),(i–k) shows microscopic images of the fabricated L-TMMS, R-TMMS, and SMMS. The arrows indicate the local displacement-vector orientation around singularities A and B: clockwise and anticlockwise rotations in the TMMS are shown in red and blue, respectively, while the SMMS displays radial, mirror-symmetric patterns depicted in green.

3. EXPERIMENTAL SETUP

3.1. Sample Preparation

A triangular lattice of silver (Ag) disks was fabricated on a 50 μm-thick Zeonor film using a printed electronics technique.[30] Two types of film were prepared: film-1 and film-2 with lattice constants of 52 and 51 μm, respectively. Each disk had a radius of approximately 11.25 μm, and the thickness was ~600 nm. A statistical analysis of 500 Ag disks yielded an average radius of 11.37 μm with a standard deviation of 0.065 μm. The lattice constant is defined by the printed-electronics mask, whose geometric precision is ±0.01 μm; thus, the lattice-pitch error is also ±0.01 μm. This configuration was chosen to realize a well-defined periodic metallic structure capable of supporting resonant interactions with THz waves. Figure 2(a) shows an optical image of film-1 along with its schematic representation, highlighting the uniform arrangement of Ag disks on the polymer substrate.

The transmission characteristics of film-1 were evaluated using THz Fourier-transform infrared spectroscopy (FTIR); the results are shown in Figure 2(b). A pronounced transmission dip appears near 4.3 THz, which corresponds to the lattice resonance associated with the periodic metallic array.[31] This resonance arises from the coupling between the incident THz waves and the collective oscillations of free electrons in the metallic disks, which is strongly influenced by the lattice constant. Consequently, the transmittance of the MMS depends not only on the refractive index of the surrounding medium but also on the resonance frequency determined by the geometric parameters of the lattice. These characteristics form the basis for tailoring the electromagnetic response of MMSs for THz applications.

The TMMS consisted of two film-1 samples with metal surfaces oriented toward one another and periodic Ag layers rotated at an angle of approximately 1.5°. In contrast, the metallic surfaces of film-1 and film-2 in the SMMS configuration both oriented inward, resulting in a moiré pattern attributable to the disparity in lattice constants. As shown in Figure 2(c), two types of MMS sample (TMMS and SMMS) were prepared by sandwiching two films between jigs. This not only enables easy adjustment of the TMMS angle but also facilitates simple reconfiguration. A pair of flexible magnetic sheets were employed as the outer holding jigs to secure the two films. These sheets were positioned outside the THz beam path, so they are not expected to distort the polarization of the incident THz radiation used in the measurements. In addition, the two metasurface layers were fabricated with printed fiducial markers such that aligning these fiducials yields a preset twist angle of approximately 1.5°. Repeated assemblies and image-based verification of the resulting moiré period indicate that the twist-angle uncertainty is on the order of ± 0.1°. The interlayer spacing was maintained below 10 μm, as confirmed by microscopic inspection, and no qualitative change in the THz-CD contrast was observed within this spacing range.

3.2. Experimental Setup

The THz-CD spectroscopic imaging experimental system employs a frequency-tunable THz source[32−35] that utilizes the nonlinear optical effects of DFG with a 4-*N*,*N*-dimethylamino-4′-*N*′-methylstilbazolium tosylate (DAST) crystal pumped by a 1.5 μm dual-wavelength source, as shown in Figure2 (d). The dual-wavelength source itself is excited by a 1 μm picosecond laser (EKSPLA FPS200; repetition rate: 1 MHz, pulse width: 8.2 ps, wavelength: 1064 nm). Wavelength λ_1 was determined to be 1.504 μm. Wavelength λ_2 was tuned from 1.504 to 1.613 μm, corresponding to a tunable THz frequency range of 2 to 15 THz, by automated control using LabVIEW. The DAST crystal used for DFG had lateral dimensions of 5 mm × 5 mm and a thickness of 0.7 mm. The THz DAST-DFG source used in this study had a spectral line width of 0.2 THz at 4 THz. The THz output from the DAST-DFG source with linear polarization was converted into a circularly polarized beam utilizing a quarter-wave plate (TYDEX, WP-CQ, at 4 THz). THz-CD spectroscopy was limited to the 3–6 THz range because of the quarter-wave plate's performance constraints. The measurement results of circular polarization ellipticity for each THz frequency are shown in Figure 2(e). Employing a Fresnel-

Downloaded from pubs.acs.org/apchd5/article-pdf/13/12/3357/6626029/acsphotonics.6c00372.pdf by NATL INST FOR MATLS SCIENCE (NIMS) user on 12 November 2026

https://doi.org/10.1021/acsphotonics.6c00372
ACS Photonics 2026, 13, 3357−3368

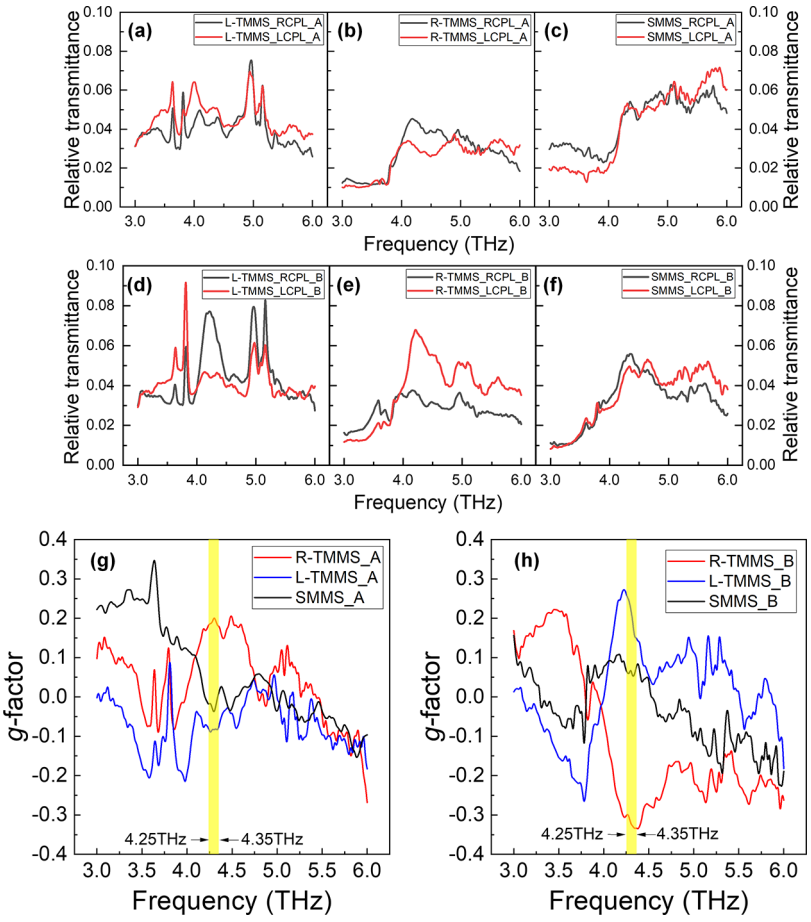


Figure 3. (a–f) Relative transmission spectra measured under RCP and LCP illumination at singularities A and B of the L-TMMS, R-TMMS, and SMMS. The spectra were obtained by recording the sample-present and sample-absent signals under identical crossed-Nicol conditions. (g, h) *g*-factor spectra at singularities A and B, respectively, calculated from the transmission spectra shown in panels (a–f).

rhomb-wave plate[36,37] composed of silicon with minimal refractive index frequency dispersion in the THz region would enable the realization of THz-CD spectroscopic imaging across all bands of the DAST-DFG source, specifically 2–15 THz. In this experiment, it was not utilized due to a decrease in the signal-to-noise ratio attributed to Fresnel loss.

A Tsurupica lens with a focal length of 50 mm was used to focus the circularly polarized THz beam onto the sample with a beam diameter of ~200 μm at 4 THz, as measured by a THz camera (NEC, T0832) and a pinhole scanning technique. The sample was mounted on a two-axis automatic stage (SIGMAKOKI, OSMS20–35(XYZ)) and could be scanned in the x–y plane. A circularly polarized crossed-Nicol configuration consisting of a quarter-wave plate and a wire-grid analyzer (AsahiKASEI, WGF, HC12N) was employed to detect only the polarization component modulated by the sample (see Figure 2(f)). The signal was identified via a cryogenic silicon bolometric detector through a lock-in amplifier (NF, LI5640). In our experiment, switching between LCP and RCP transmission measurements is performed simply by rotating the two quarter-wave plates and the wire-grid analyzer in the crossed-Nicol configuration, without adjusting any other optical components. Under this arrangement, the bolometer detects only the polarization component generated or modified by the sample, because nonconverted components are suppressed by the analyzer. Although the incident circular polarization is not ideal, with an ellipticity of approximately 0.8 at 4.3 THz, such deviations contribute negligibly to the detected signal under this geometry. Consequently, the measured *g*-factor predominantly reflects the sample-induced chiroptical response, and the observed sign inversion and spatial contrast arise from the intrinsic THz-CD interaction rather than from polarization impurity.

The THz-CD spectroscopy measurement involved the irradiation of a circularly polarized beam at specific locations (singularities A and B) on the TMMS and SMMS samples while the frequency was tuned from 3 to 6 THz. The spectroscopic results were calculated using the dissymmetry factor (*g*-factor) determined from the transmission results of the LCP and RCP beams. The *g*-factor is expressed as

$$g = (I_R - I_L)/(I_R + I_L) \quad (1)$$

where I_L and I_R denote the transmitted intensity for the LCP and RCP beams, respectively. In the THz-CD imaging, the frequency at which differences in THz-CD signals occurred was fixed, circularly polarized beam (both LCP and RCP) was employed, and the sample was raster scanned for imaging and subsequently replotted using the *g*-factor.

4. RESULTS

We now present the results of THz-CD spectroscopy and imaging. Figure 3 shows the THz-CD spectra alongside the corresponding optical images (Figure 4) for L-TMMS, R-TMMS, and SMMS samples. The TMMS samples exhibit a distinct inversion of the *g*-factor near 4.3 THz, indicating separate THz-CD responses arising from the opposite 3D chiralities of the structures.

4.1. THz-CD Spectroscopy

Figure 3 summarizes the THz-CD spectroscopic measurements around singularities A and B for L-TMMS, R-TMMS, and SMMS samples. Relative transmission spectra measured at six locations—namely, for RCP and LCP illumination at singularities A and B of both L-TMMS and R-TMMS, as well

Downloaded from pubs.acs.org/apchd5/article-pdf/13/12/3357/6626029/acsphotonics.6c00372.pdf by NATL INST FOR MATLS SCIENCE (NIMS) user on 12 November 2026

https://doi.org/10.1021/acsphotonics.6c00372
ACS Photonics 2026, 13, 3357–3368

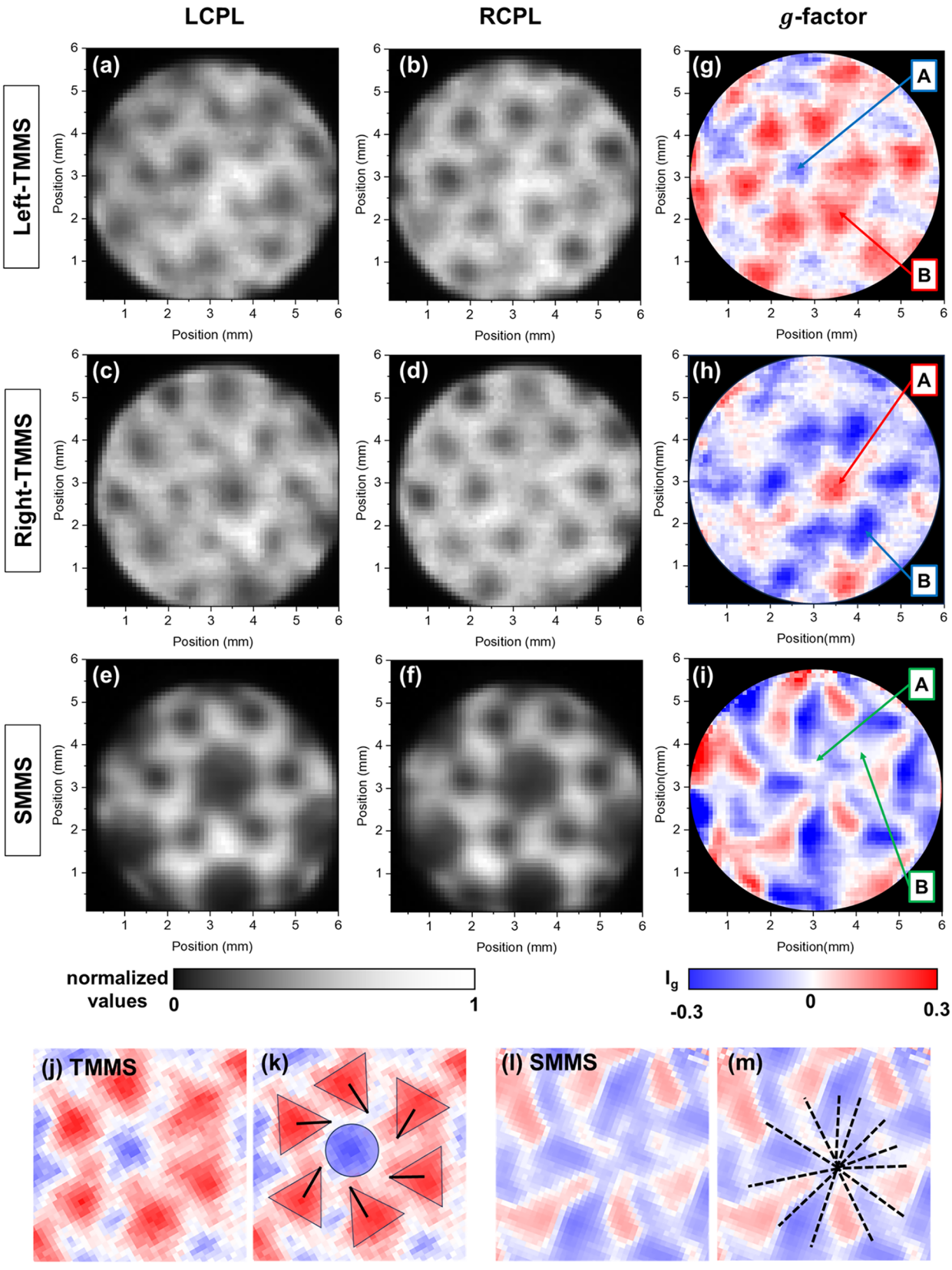


Figure 4. THz polarization and circular dichroism (THz-CD) imaging of L-TMMS, R-TMMS, and SMMS at 4.3 THz. The scanned area is 6 mm × 6 mm with 60 × 60 pixels (100 μm per pixel). (a–f) Polarization-resolved THz intensity images under LCP and RCP illumination, showing singularities as localized dark regions. (g–i) Corresponding THz-CD images derived from the polarization dichroism *g*-factor. (j) Enlarged view of panel (g), showing the detailed TMMS features around singularities A and B. (k) Schematic eye guide corresponding to panel (j), illustrating the characteristic circular and triangular patterns. (l) Enlarged view of panel (i), highlighting the SMMS response in the vicinity of singularity A. (m) Schematic eye guide corresponding to panel (l), emphasizing the radial, mirror-symmetric configuration.

https://doi.org/10.1021/acsphotonics.6c00372
ACS Photonics 2026, 13, 3357–3368

Downloaded from pubs.acs.org/apchd5/article-pdf/13/12/3357/6626029/acsphotonics.6c00372.pdf by NATL INST FOR MATLS SCIENCE (NIMS) user on 12 November 2026

as at the corresponding singularities of the SMMS—were obtained by recording the sample-present signals under the crossed-Nicol conditions and the sample-absent reference signals under the parallel-Nicol configuration (Figure 3(a)–(f)). These spectra allow direct comparison of the absolute transmitted intensities and the contrast between RCP and LCP illumination at each position, thereby clarifying how the observed *g*-factor arises from the underlying structural chirality. Pronounced spin-dependent transmission differences are observed for the TMMS near 4.3 THz, whereas the SMMS exhibits nearly overlapping RCP/LCP transmission at both singularities, consistent with its achiral character.

For singularity A (Figure 3(g)), the R-TMMS exhibits a positive value of the *g*-factor at 4.3 THz, whereas the L-TMMS shows the opposite sign. This observation correlates with the rotation direction of the displacement vector $\boldsymbol{\nu}$ illustrated in Figure 1(f),(g), indicating that singularity A acts as the rotational center of the stacked layers. Figure 1(a) schematically depicts the arrangement of metallic disks around singularity A. As described in Section 2, the vector $\boldsymbol{\nu}$ in the L-TMMS rotates counterclockwise around singularity A from the orange disk in the first layer toward the light-blue disk in the second layer, while in the R-TMMS rotates clockwise around singularity A. The corresponding optical images (Figure 1(i),(j)) confirm the presence of 3D structural chirality around singularity A. The experimentally obtained THz-CD spectra thus reflect this intrinsic 3D chirality. In contrast, at singularity B (Figure 3(h)), the *g*-factor appears with the opposite sign compared to that for singularity A, consistent with the reversed rotation direction of the TMMS structure at this location. Conversely, the SMMS exhibits no significant THz-CD response at either singularity. As shown in Figure 3 (g),(h), the *g*-factor remains nearly zero at 4.3 THz, indicating negligible chirality-dependent behavior. The displacement vector $\boldsymbol{\nu}$ around the singularities of the SMMS does not form the rotational pattern observed for the TMMS. Instead, as illustrated in Figure 1(b),(k), the vectors diverge from singularity A or converge at singularity B, demonstrating mirror symmetry and the absence of chirality. The lack of detectable CD signals in the SMMS confirms the absence of inherent 3D structural chirality. Although the SMMS is achiral at the singularities A and B, small nonzero *g*-values appear away from these points. These residual signals are not associated with structural chirality at the singularities; rather, they arise because the SMMS still exhibits multiscale spatial variations in its displacement-vector field across the moiré lattice. When probed with a finite-sized THz beam, these variations yield localized $\pm g$ responses consistent with the combined chirality indicator introduced in our framework.

4.2. THz-CD Imaging

Figure 4 summarizes the experimental results of THz polarization and THz-CD imaging for L-TMMS, R-TMMS, and SMMS at 4.3 THz. The scanned region covers 60 × 60 pixels with a spatial resolution of 100 μm per pixel, corresponding to an imaging area of 6 mm × 6 mm. Figure 4(a–f) present polarization-resolved THz intensity images under LCP and RCP beams. In both the TMMS and SMMS, singularities appear as localized dark regions, indicating minimal polarization transmission. At singularities A and B, slight intensity differences suggest differential modulation of local displacement vectors depending on the incident polarization handedness. However, these differences alone do not clearly distinguish singularity A from singularity B.

To clarify these features, CD images were derived by calculating the *g*-factor from the difference in THz responses under LCP and RCP excitation (Figure 4(g–i)). For the L-TMMS (Figure 4(g)), the sign of *g* inverts between singularities A and B, reflecting the structure's chiral nature: singularity A shows a negative *g* (blue), while singularity B shows a positive *g* (red). This inversion agrees with the spectroscopic results in Figure 3, where regions with anticlockwise displacement vectors respond preferentially to LCP light (negative *g*), and clockwise vectors to RCP light (positive *g*). The shapes around singularities A and B in the *g*-factor image shown in Figure 4(g) exhibit geometries resembling a circle and a triangle, respectively. A similar contrast pattern is observed for the R-TMMS (Figure 4(h)), with the signs reversed, consistent with opposite handedness. A slight asymmetry between the positive and negative *g*-factor regions in Figure 4(g,h) can be observed. This tendency is already visible in the spectroscopic data of Figure 3: at 4.3 THz, singularity A consistently exhibits a smaller $|g|$ value than singularity B for both LCP and RCP illumination. Because the *g*-map in Figure 4(g,h) are displayed with a fixed contrast range, this difference in magnitude appears as unequal areas. Adjusting the color scale yields nearly symmetric regions around A and B. This behavior is consistent with the relative transmission spectra, which shows that the transmittance at A is lower than at B.

For clarity, Figure 4(j) shows an enlarged view of the experimental results (Figure 4(g),(k)) includes an eye guide for the circular and triangular geometries. The six triangles at singularity B are arranged to enclose a blue circle of singularity A. As shown in Figure 4(k), straight lines drawn from the centers of these triangles to their nearest vertices converge toward A. While this interpretation may be subjective, these lines suggest a pattern that appears not radial but rather twisting around singularity A.

Polarization imaging of the SMMS (Figure 4(e,f)) reveals singularities A and B and their size difference. In contrast to the TMMS, the THz-CD image of the SMMS (Figure 4(i)) shows no clear sign inversion at these singularity points; instead, *g* remains near zero (white), indicating comparable responses to both polarizations. One notable feature of the *g*-factor image for the SMMS is the radial extension of white lines originating from singularity A. Similar to the TMMS case, enlarged views and corresponding eye guides are shown in Figure 4(l,m), where 12 radial dotted lines centered on singularity A, with a *g*-factor value close to zero, can be observed. This suggests the absence of structural chirality around SMMS singularities, consistent with the spectroscopic data. Localized CD signals detected at positions other than the SMMS singularities exhibit finite values.

These results confirm that stacked Ag disk arrays in the TMMS form 3D chiral structures around singularities A and B. Notably, these chiral conformations coexist within the same in-plane framework, with local handedness switching across regions. The ability of THz-CD spectroscopy to resolve such spatially varying chirality highlights its sensitivity to 3D structural asymmetry embedded in planar metasurface designs.

5. DISCUSSION

The MMSs investigated in this study exhibit chirality arising from the relative spatial arrangement of lattice points and twist

Downloaded from pubs.acs.org/apchd5/article-pdf/13/12/3357/6260299/acsphotonics.6c00372.pdf by NATL INST FOR MATLS SCIENCE (NIMS) user on 12 November 2026

https://doi.org/10.1021/acsphotonics.6c00372
ACS Photonics 2026, 13, 3357−3368

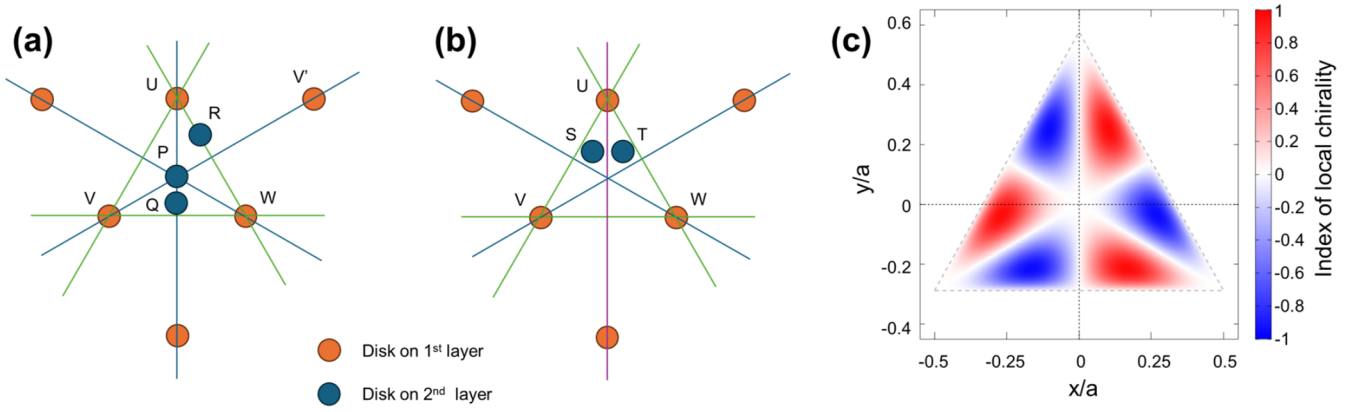


Figure 5. Local structural chirality arising from relative position of second-layer disk within unit cell of first-layer triangular lattice. (a) When the second-layer disk lies on a mirror symmetry axis, the configuration is locally achiral, and the chirality indicator is zero. (b) When the disk is displaced from the symmetry axis, the chirality indicator becomes nonzero. Points S and T, which are mirror-symmetric with respect to the purple line, exhibit chirality of opposite signs. (c) Spatial distribution of local chirality indicator $L(x, y)$ as defined by (eq 2).

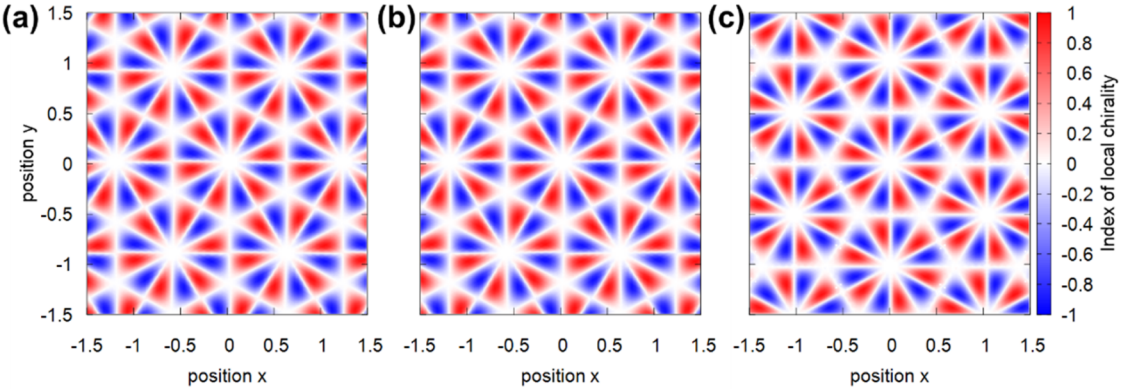


Figure 6. Spatial distribution of local chirality indicator $L(x,y)$ for various moiré configurations. (a) Clockwise twisted-layer moiré with rotation angle of $\frac{\theta}{2} = 0.02$ rad. (b) Anticlockwise twisted-layer moiré with $\frac{\theta}{2} = -0.02$ rad. (c) Scale moiré with 4% lattice expansion.

between two layers of disk arrays. This structural chirality influences the interaction with incident THz beams, giving rise to CD signals. Here, we discuss the chirality characteristics of the TMMS and SMMS configurations, focusing on indicators of local and macroscopic chirality.

5.1. Local Chirality

As illustrated in Figure 5, we consider a unit cell formed by three disks arranged in a triangular lattice (points U, V, and W) in the first layer and analyze the chirality induced by the placement of a second-layer disk within this cell. When the second-layer disk is located at point P (the centroid of triangle UVW), the unit cell possesses three mirror symmetry axes passing through P, resulting in an achiral configuration. Similarly, placing the disk at point Q, located on the perpendicular bisector of triangle UVW, yields a mirror-symmetric and achiral structure. Point R, situated on one of the triangle's edges (e.g., UW), also corresponds to a mirror-symmetric configuration due to the reflection symmetry between adjacent unit cells (UVW and UV'W).

In contrast, when the second-layer disk is placed at point S, which lies off these symmetry axes, the unit cell lacks mirror symmetry and exhibits local chirality. Point T, the mirror-symmetric counterpart of S with respect to the perpendicular bisector, also exhibits chirality, but with opposite handedness. Based on these observations, we propose that a suitable chirality indicator should approach zero near symmetry axes and increase with distance from them, with sign inversion across mirror-symmetric positions. To quantify this behavior, we define the following chirality function

$$L(x, y) = k\left\{\frac{2}{(\sqrt{3}a)^3}y(y^2 - 3x^2) - \frac{1}{(\sqrt{3}a)^2}(x^2 + y^2) + \frac{1}{3^3}\right\}\cdot\left\{\frac{2}{(\sqrt{3}a)^3}y(y^2 - 3x^2) + \frac{2}{(\sqrt{3}a)^2}(x^2 + y^2) - \frac{2^3}{3^3}\right\}\cdot\left\{\frac{2}{a^3}x(x^2 - 3y^2)\right\} \quad (2)$$

Here, k is a proportionality constant. The chirality function is defined within a regular triangle UVW of side length a, with its centroid P set as the origin. The x-axis aligns parallel to edge VW and the y-axis follows the direction from P to point U. As shown in Figure 5(c), the value of $L(x, y)$ depends on the position of the second-layer disk, reflecting the local chirality of each unit cell. The formulation of (eq 2) is based on the considerations of chirality on spherical surfaces presented in ref 38 where a cubic harmonic function $K_9^4(x, y, z)$ defined on an octant of a sphere was projected onto a planar triangular domain. Figure 6 presents the spatial distribution of this indicator for various moiré configurations arising in triangular lattices (twisted-layer and scale). While similar patterns emerge

https://doi.org/10.1021/acsphotonics.6c00372
ACS Photonics 2026, 13, 3357−3368

Downloaded from pubs.acs.org/apchd5/article-pdf/13/12/3357/6260299/acsphotonics.6c00372.pdf by NATL INST FOR MATLS SCIENCE (NIMS) user on 12 November 2026

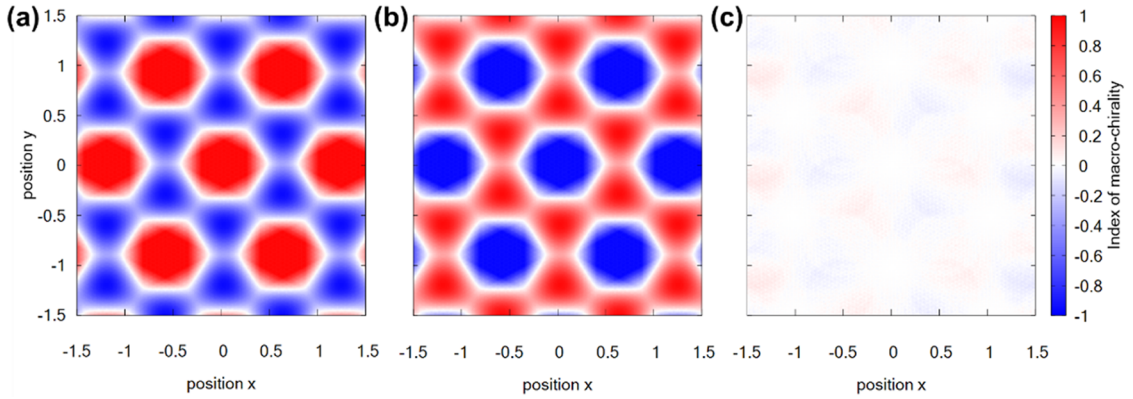


Figure 7. Spatial distribution of macroscopic chirality indicator $M(r_0)$ for various moiré configurations calculated with beam diameter of $R = 8a$. The values of $M(r_0)$ are normalized such that the maximum and minimum are +1 and −1, respectively. (a) Clockwise twisted-layer moiré ($\frac{\theta}{2} = +0.02$ rad). (b) Anticlockwise twisted-layer moiré ($\frac{\theta}{2} = -0.02$ rad). (c) Scale moiré with 4% expansion.

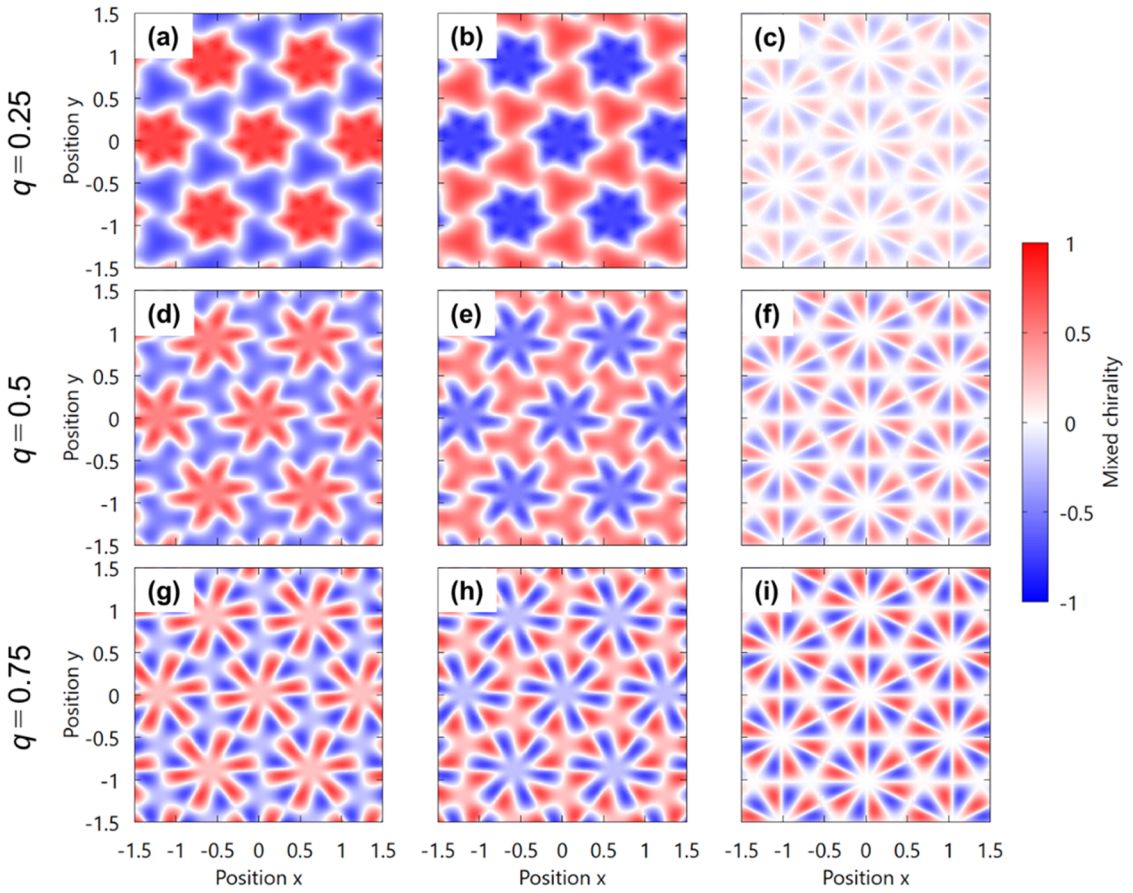


Figure 8. Spatial distribution of combined chirality indicator $C(x,y)$ for mixing ratios of (a−c) $q = 0.25$, (d−f) $q = 0.5$, and (g−i) $q = 0.75$. (a, d, g) Clockwise twisted-layer moiré ($\frac{\theta}{2} = +0.02$ rad). (b, e, h) Anticlockwise twisted-layer moiré ($\frac{\theta}{2} = -0.02$ rad). (c, f, i) Scale moiré with 4% expansion.

regardless of the displacement type, the experimentally observed differences cannot be fully explained by this local chirality indicator alone.

5.2. Macroscopic Chirality

The moiré patterns studied here include various twisting-layer and scale configurations, each imparting distinct spatial distributions of local displacement vector rotation, as shown in Figure 1. These distributions influence the interaction with incident THz beams. To characterize the degree of such macroscopic twist, we define the following indicator

$$M(\boldsymbol{r}_0) = \frac{1}{S}\int\int_{|r|<R} \boldsymbol{v}(\boldsymbol{r}) \times (\boldsymbol{r} - \boldsymbol{r}_0)\mathrm{d}\boldsymbol{r} \tag{3}$$

Here, R denotes the beam diameter, $\boldsymbol{v}(\boldsymbol{r})$ is the local displacement vector at position $\boldsymbol{r}$, and S is the beam-illuminated area. This quantity represents the integrated rotational behavior of the vector field around the beam center

https://doi.org/10.1021/acsphotonics.6c00372
ACS Photonics 2026, 13, 3357−3368

Downloaded from pubs.acs.org/apchd5/article-pdf/13/12/3357/6260299/acsphotonics.6c00372.pdf by NATL INST FOR MATLS SCIENCE (NIMS) user on 12 November 2026

r_0, with its sign indicating the direction of rotation. Figure 7 shows the in-plane distribution of $M(r_0)$ for each moiré configuration under the assumption that the beam diameter is eight times the unit cell size. For twisted-layer moiré structures, finite values of M are observed near singularities A and B, with opposite signs. The sign also reverses between left- and right-handed configurations. In contrast, scale moiré structures do not exhibit significant values of M, indicating the absence of macroscopic chirality. Figure 7 demonstrates pronounced symmetry between points A and B, in contrast to the experimental data in Figure 4(g,h), which show considerably poorer symmetry compared with the model results.

5.3. Multiscale Chirality (Combined Chirality Indicator)

The incident beam is expected to respond to both local and macroscopic chirality, as both contribute to the spatial modulation of the electromagnetic field. To account for this, we define the following combined chirality indicator

$$C(x, y) = qL(x, y) + (1 - q)M(x, y) \quad (4)$$

where $q \in [0, 1]$ is a mixing parameter. Figure 8 illustrates the spatial distribution of $C(x, y)$. A 6-fold symmetric snowflake-like pattern emerges around singularity A, while a 3-fold symmetric pattern appears near singularity B. These patterns reflect the loss of mirror symmetry due to the interplay between local and macroscopic chirality. A comparison with experimental results suggests that a mixing ratio of $q = 0.25$ yields patterns that are most consistent with observations. As shown in Figure 5, the TMMS exhibits twisted geometries, while the SMMS exhibits radial configurations. This finding indicates that THz beams sense composite chirality contributions that go beyond what local or macroscopic indicators can individually describe.

Because the measured g-factor reflects both the local displacement-vector–induced chirality and the spatial averaging by the finite THz beam, different choices of moiré geometry and beam-scale conditions naturally generate different chiral-domain patterns. Adjusting parameters such as the twist-induced displacement-vector distribution or the relative scale between the moiré structure and the THz beam provides a conceptual means to tailor the spatial chirality map. Although quantitative optimization is beyond the scope of this study, the present results offer a clear path toward flexible design of chirality distributions in moiré-based photonic systems. Such capability could support future applications, including site-resolved THz-CD mapping of chiral domains in biomolecular or soft-matter assemblies, or the development of customized circular-polarization elements based on moiré-induced chirality.

6. CONCLUSION

We have established a frequency-tunable THz-CD spectroscopic imaging platform that operates across 3–6 THz with narrowband, polarization-pure (spin-selective) excitation and a two-dimensional readout, thereby converting THz-CD from a spatially averaged spectral probe into a site-resolved imaging modality. Using TMMSs as a deterministic, top-down model and SMMSs as an achiral control, we directly map structural chirality and show that the dissymmetry (g-factor) inverts sign between topological singularities within a single planar architecture and reverses with the global twist handedness, whereas SMMS counterparts remain near zero—demonstrating the sensitivity and selectivity of spin-based THz imaging.

Beyond visualization, we provide experimental validation of a multiscale description for the THz chiroptical response. Specifically, we formulate complementary indicators that quantify local displacement asymmetry (unit-cell scale) and macroscopic rotational geometry (beam-integrated field) and demonstrate that only their combined action reproduces the measured 2D THz-CD images. This result clarifies that a single-scale proxy is insufficient in this frequency range and supplies a quantitative framework for interpreting spatial THz-CD contrasts in engineered metasurface architectures.

Taken together, these findings position spatial THz-CD imaging (3–6 THz) as a practical metrology for designing, controlling, and benchmarking multiscale chirality in planar architectures. By providing deterministic, reconfigurable model systems and a high-fidelity imaging tool, our approach complements bottom-up self-assembled chiral matter—where accessible geometries and spatial registries are often constrained—and enables site-specific chiral characterization relevant to metasurfaces, soft-phonon materials,[25] and biomolecular assemblies. We anticipate that extending the platform across the broader 2–15 THz range and refining polarization optics will further expand its reach, opening avenues for quantitative chiral photonics and advanced materials diagnostics[39−42] in the THz regime.

AUTHOR INFORMATION

Corresponding Author

Katsuhiko Miyamoto − *Graduate School of Engineering, Chiba University, Chiba 263-8522, Japan; Molecular Chirality Research Center, Chiba University, Chiba 263-8522, Japan;* orcid.org/0000-0002-2611-882X; Email: k-miyamoto@faculty.chiba-u.jp

Authors

Uina Chiba − *Graduate School of Engineering, Chiba University, Chiba 263-8522, Japan*

Shota Tsuji − *Graduate School of Engineering, Chiba University, Chiba 263-8522, Japan*

Gaku Oritani − *Graduate School of Engineering, Chiba University, Chiba 263-8522, Japan*

Takumi Yoichi − *Graduate School of Engineering, Chiba University, Chiba 263-8522, Japan*

Rinpei Sasaki − *Graduate School of Engineering, Chiba University, Chiba 263-8522, Japan*

Takeo Minari − *Research Center for Functional Materials, National Institute for Materials Science, Tsukuba, Ibaraki 305-0044, Japan;* orcid.org/0000-0001-7690-221X

Seigo Ohno − *Department of Physics, Tohoku University, Sendai 980-8578, Japan*

Complete contact information is available at: https://pubs.acs.org/10.1021/acsphotonics.6c00372

Author Contributions

The manuscript was written through contributions of all authors. All authors have given approval to the final version of the manuscript.

Funding

JSPS KAKENHI (grant numbers JP23K23248, JP24KK0108, JP22K18979, and JP23K04567) and JST FOREST Program (grant number JPMJFR2036).

Downloaded from pubs.acs.org/apchd5/article-pdf/13/12/3357/6260299/acsphotonics.6c00372.pdf by NATL INST FOR MATLS SCIENCE (NIMS) user on 12 November 2026

Notes

The authors declare no competing financial interest.

■ ACKNOWLEDGMENTS

The authors would like to thank Prof. Takashige Omatsu at Chiba University for useful discussions. The authors would also like to thank Prof. Koji Suizu at Chiba Institute of Technology for providing the THz camera. The authors are grateful to Dr. Hirohisa Uchida (Hamamatsu Photonics K.K.) for kindly providing the DAST crystal used in this study.

■ REFERENCES

(1) Choi, W. J.; Kim, J. Y.; Hwang, M.; Lim, C. M.; Park, B. C.; Emre, A.; Lee, S. H.; Kotov, N. A. Highly Elliptic Circular Dichroism of Copper Aspartate One-Dimensional Nanostructures across the Ultraviolet to Terahertz Ranges. *Nano Lett.* **2025**, *25* (19), 7699−7706.

(2) Berova, N.; Di Bari, L.; Pescitelli, G. Application of Electronic Circular Dichroism in Configurational and Conformational Analysis of Organic Compounds. *Chem. Soc. Rev.* **2007**, *36* (6), 914−931.

(3) Hao, C.; Gao, R.; Li, Y.; Xu, L.; Sun, M.; Xu, C.; Kuang, H. Chiral Semiconductor Nanoparticles for Protein Catalysis and Profiling. *Angew. Chem.* **2019**, *131* (22), 7449−7452.

(4) Park, K. H.; Kwon, J.; Jeong, U.; Kim, J. Y.; Kotov, N. A.; Yeom, J. Broad Chiroptical Activity from Ultraviolet to Short-Wave Infrared by Chirality Transfer from Molecular to Micrometer Scale. *ACS Nano* **2021**, *15* (9), 15229−15237.

(5) Wu, Z.; Zheng, Y. Moiré Chiral Metamaterials. *Adv. Opt. Mater.* **2017**, *5* (16), No. 1700034.

(6) Formen, J. S. S. K.; Nelson, E.; Wolf, C. Molecular Sensing of Chiral Carboxylic Acid Enantiomers Using CD Inductions in the Visible Light Region. *J. Org. Chem.* **2025**, *90* (2), 994−1000.

(7) Yan, J.; Feng, W.; Kim, J. Y.; Lu, J.; Kumar, P.; Mu, Z.; Wu, X.; Mao, X.; Kotov, N. A. Self-Assembly of Chiral Nanoparticles into Semiconductor Helices with Tunable near-Infrared Optical Activity. *Chem. Mater.* **2020**, *32* (1), 476−488.

(8) Kwon, J.; Park, K. H.; Choi, W. J.; Kotov, N. A.; Yeom, J. Chiral Spectroscopy of Nanostructures. *Acc. Chem. Res.* **2023**, *56* (12), 1359−1372.

(9) Arita, Y.; Simpson, S. H.; Bruce, G. D.; Wright, E. M.; Zemánek, P.; Dholakia, K. Cooling the Optical-Spin Driven Limit Cycle Oscillations of a Levitated Gyroscope. *Commun. Phys.* **2023**, *6* (1), No. 238.

(10) Choi, W. J.; Lee, S. H.; Park, B. C.; Kotov, N. A. Terahertz Circular Dichroism Spectroscopy of Molecular Assemblies and Nanostructures. *J. Am. Chem. Soc.* **2022**, 22789−22804.

(11) Chen, C.; Yan, Z. S.; Ma, Y. Q.; Ding, H. M. Effect of Terahertz Waves on the Structure of the Aβ42 Monomer, Dimer, and Protofibril: Insights from Molecular Dynamics Simulations. *ACS Chem. Neurosci.* **2023**, *14* (23), 4128−4138.

(12) Zhang, J.; Zhu, Z.; Wu, Y.; Ji, T.; Wang, J.; Zhu, H.; Peng, W.; Chen, M.; Li, S.; Zhao, H. Broadband Terahertz Spectroscopy and Weak Interactions of Adenosine with Vibrational Mode Analysis. *J. Infrared, Millimeter, Terahertz Waves* **2023**, *44* (11−12), 814−829.

(13) Choi, W. J.; Cheng, G.; Huang, Z.; Zhang, S.; Norris, T. B.; Kotov, N. A. Terahertz Circular Dichroism Spectroscopy of Biomaterials Enabled by Kirigami Polarization Modulators. *Nat. Mater.* **2019**, 820−826.

(14) Talkington, S.; Mele, E. J. Terahertz Circular Dichroism in Commensurate Twisted Bilayer Graphene. *Phys. Rev. B* **2023**, *108* (8), No. 085421.

(15) Frenzel, M.; Urban, J. M.; Nest, L.; Kampfrath, T.; Spencer, M. S.; Maehrlein, S. F. Quartz as an Accurate High-Field Low-Cost THz Helicity Detector. *Optica* **2024**, *11* (3), 362−370.

(16) Deng, Q.-M.; Li, X.; Hu, M.-X.; Li, F.-J.; Li, X.; Deng, Z.-L. Advances on Broadband and Resonant Chiral Metasurfaces. *npj Nanophotonics* **2024**, *1* (1), No. 20.

(17) Pan, F.; Li, X.; Johnson, A. C.; Dhuey, S.; Saunders, A.; Hu, M.-X.; Dixon, J. P.; Dagli, S.; Lau, S.-C.; Weng, T.; Chen, C.-Y.; Zeng, J.-H.; Apte, R.; Heinz, T. F.; Liu, F.; Deng, Z.-L.; Dionne, J. A. Room-Temperature Valley-Selective Emission in Si-MoSe2 Heterostructures Enabled by High-Quality-Factor Chiroptical Cavities. *Nat. Commun.* **2026**, *17* (1), No. 20.

(18) Li, H.; Li, G.; Deng, Z.; Xu, W.; Xu, H.; Li, J.; Song, C.; Qiu, F.; Zhang, Y.; Ren, Y.; Yao, J. Multifunctional All-Silicon Terahertz Chiral Metasurfaces via Integrated Moiré and Spin-Decoupled Phase Engineering. *Laser Photon. Rev.* **2026**, No. e03260.

(19) Choi, W. J.; Yano, K.; Cha, M.; Colombari, F. M.; Kim, J.-Y.; Wang, Y.; Lee, S. H.; Sun, K.; Kruger, J. M.; de Moura, A. F.; Kotov, N. A. Chiral Phonons in Microcrystals and Nanofibrils of Biomolecules. *Nat. Photonics* **2022**, *16* (5), 366−373.

(20) Chen, H.; Wu, W.; Zhu, J.; Yang, S. A.; Zhang, L. Propagating Chiral Phonons in Three-Dimensional Materials. *Nano Lett.* **2021**, *21*, 3060−3065.

(21) Yeom, J.; Santos, U. S.; Chekini, M.; Cha, M.; De Moura, A. F.; Kotov, N. A. Chiromagnetic Nanoparticles and Gels. *Science* **2018**, *359*, 309−314.

(22) Oishi, E.; Fujii, Y.; Koreeda, A. Selective Observation of Enantiomeric Chiral Phonons in α -Quartz. *Phys. Rev. B* **2024**, *109* (10), No. 104306.

(23) Elgabarty, H.; Kampfrath, T.; Bonthuis, D. J.; Balos, V.; Kaliannan, N. K.; Loche, P.; Netz, R. R.; Wolf, M.; Kühne, T. D.; Sajadi, M. Energy Transfer within the Hydrogen Bonding Network of Water Following Resonant Terahertz Excitation. *Sci. Adv.* **2020**, *6* (17), No. eaay7074.

(24) Begušić, T.; Blake, G. A. Two-Dimensional Infrared-Raman Spectroscopy as a Probe of Water's Tetrahedrality. *Nat. Commun.* **2023**, *14* (1), No. 1950.

(25) Basini, M.; Pancaldi, M.; Wehinger, B.; Udina, M.; Unikandanunni, V.; Tadano, T.; Hoffmann, M. C.; Balatsky, A. V.; Bonetti, S. Terahertz Electric-Field-Driven Dynamical Multiferroicity in SrTiO3. *Nature* **2024**, *628* (8008), 534−539.

(26) Yu, N.; Genevet, P.; Kats, M. A.; Aieta, F.; Tetienne, J.-P.; Capasso, F.; Gaburro, Z. Light Propagation with Phase Discontinuities: Generalized Laws of Reflection and Refraction. *Science* **2011**, *334* (6054), 333−337.

(27) Miyamaru, F.; Hangyo, M. Anomalous Terahertz Transmission through Double-Layer Metal Hole Arrays by Coupling of Surface Plasmon Polaritons. *Phys. Rev. B* **2005**, *71* (16), No. 165408.

(28) Ohno, S. Projection of Phase Singularities in Moiré Fringe onto a Light Field. *Appl. Phys. Lett.* **2016**, *108* (25), No. 251104.

(29) Ohno, S.; Hoshina, H.; Minamide, H.; Ishihara, T.*Phase Singularities in Moiré Type Metasurfaces*; Progress In Electromagnetics Research Symposium; IEEE, 2018; pp 2023−2026.

(30) Li, L.; Li, W.; Sun, Q.; Liu, X.; Jiu, J.; Tenjimbayashi, M.; Kanehara, M.; Nakayama, T.; Minari, T. Dual Surface Architectonics for Directed Self-Assembly of Ultrahigh-Resolution Electronics. *Small* **2021**, *17* (26), No. 2101754.

(31) Lee, H.-S.; Hwang, G.-W.; Seong, T.-Y.; Park, J.; Kim, J. W.; Kim, W. M.; Kim, I.; Lee, K.-S. Design of Mid-Infrared Filter Array Based on Plasmonic Metal Nanodiscs Array and Its Application to on-Chip Spectrometer. *Sci. Rep.* **2021**, *11* (1), No. 12218.

(32) Miyamoto, K.; Sano, K.; Miyakawa, T.; Niinomi, H.; Toyoda, K.; Vallés, A.; Omatsu, T. Generation of High-Quality Terahertz OAM Mode Based on Soft-Aperture Difference Frequency Generation. *Opt. Express* **2019**, *27* (22), No. 31840.

(33) Ohno, S.; Miyamoto, K.; Minamide, H.; Ito, H. New Method to Determine the Refractive Index and the Absorption Coefficient of Organic Nonlinear Crystals in the Ultra-Wideband THz Region. *Opt. Express* **2010**, *18* (16), 17306−17312.

(34) Miyamoto, K.; Suizu, K.; Akiba, T.; Omatsu, T. Direct Observation of the Topological Charge of a Terahertz Vortex Beam Generated by a Tsurupica Spiral Phase Plate. *Appl. Phys. Lett.* **2014**, *104* (26), No. 261104.

Downloaded from pubs.acs.org/apchd5/article-pdf/13/12/3357/6626029/acsphotonics.6c00372.pdf by NATL INST FOR MATLS SCIENCE (NIMS) user on 12 November 2026

https://doi.org/10.1021/acsphotonics.6c00372
ACS Photonics 2026, 13, 3357−3368

(35) Miyamoto, K.; Lee, A.; Saito, T.; Akiba, T.; Suizu, K.; Omatsu, T. Broadband Terahertz Light Source Pumped by a 1 Mm Picosecond Laser. *Appl. Phys. B* **2013**, *110* (3), 321−326.
(36) Kawada, Y.; Yasuda, T.; Nakanishi, A.; Akiyama, K.; Hakamata, K.; Takahashi, H. Achromatic Prism-Type Wave Plate for Broadband Terahertz Pulses. *Opt. Lett.* **2014**, *39* (9), 2794−2797.
(37) Mou, S.; D'Arco, A.; Tomarchio, L.; Macis, S.; Petrarca, M.; Lupi, S. Achromatic Terahertz Quarter-Wave Fresnel Rhomb Retarder. *Appl. Phys. Lett.* **2023**, *122* (24), No. 241102.
(38) Abdelmaqsoud, K.; Radetic, M.; Fernández-Cabán, C.; Widom, M.; Kitchin, J. R.; Gellman, A. J. Structure Sensitive Reaction Kinetics of Chiral Molecules on Intrinsically Chiral Surfaces. *J. Phys. Chem. C* **2024**, *128* (33), 13879−13887.
(39) Zhao, J.; Zhang, L.; Liang, H. Advances in Metasurface-Based Terahertz Sensing. *Adv. Phys. Res.* **2024**, *3* (12), No. 2400077.
(40) Banks, P. A.; Kleist, E. M.; Ruggiero, M. T. Investigating the Function and Design of Molecular Materials through Terahertz Vibrational Spectroscopy. *Nat. Rev. Chem.* **2023**, *7*, 480−495.
(41) Li, X.; Bamba, M.; Zhang, Q.; Fallahi, S.; Gardner, G. C.; Gao, W.; Lou, M.; Yoshioka, K.; Manfra, M. J.; Kono, J. Vacuum Bloch-Siegert Shift in Landau Polaritons with Ultra-High Cooperativity. *Nat. Photonics* **2018**, *12* (6), 324−329.
(42) Matsuda, T.; Higo, T.; Koretsune, T.; Kanda, N.; Hirai, Y.; Peng, H.; Matsuo, T.; Yoshikawa, N.; Shimano, R.; Nakatsuji, S.; Matsunaga, R. Ultrafast Dynamics of Intrinsic Anomalous Hall Effect in the Topological Antiferromagnet Mn_3Sn. *Phys. Rev. Lett.* **2023**, *130*, No. 126302.

Downloaded from pubs.acs.org/apchd5/article-pdf/13/12/3357/6260299/acsphotonics.6c00372.pdf by NATL INST FOR MATLS SCIENCE (NIMS) user on 12 November 2026

https://doi.org/10.1021/acsphotonics.6c00372
ACS Photonics 2026, 13, 3357−3368